Letter

Weak superfluidity in twisted optical potentials

Dean Johnstone [1], Shanya Mishra [1], Zhaoxuan Zhu [1], Hepeng Yao [2], and Laurent Sanchez-Palencia [1]
[1]*CPHT, CNRS, Ecole Polytechnique, IP Paris, F-91128 Palaiseau, France*
[2]*DQMP, University of Geneva, 24 Quai Ernest-Ansermet, CH-1211 Geneva, Switzerland*

(Received 18 June 2024; revised 9 October 2024; accepted 28 November 2024; published 23 December 2024)

A controlled twist between separate potentials can drastically influence localization properties of quantum particles between ordered and (quasi)disordered limits. Transport properties of single-particle and correlated fermionic materials have been extensively studied in connection with twisted bilayer graphene, but their bosonic counterpart remains largely unexplored. Here, we study bosonic matter in twisted potentials. We use continuous-space quantum Monte Carlo simulations to determine the unique phase diagrams of strongly correlated ultracold bosons in twisted optical lattices. For commensurate twisting angles, spectral gaps govern the formation of insulators, separated by thin superfluid domains. These domains form weak superfluids; with low superfluid fraction at zero temperature and high sensitivity to thermal fluctuations, but may be stabilized under appropriate parameter control. In contrast, slightly changing the twisting angle to an incommensurate value destroys most spectral gaps, leaving behind a prominent Bose glass phase. Our results are directly applicable to current generation experiments that quantum simulate moiré physics.

DOI: 10.1103/PhysRevResearch.6.L042066

Introduction. In the field of condensed matter, strongly correlated materials exhibit exotic phase transitions and entanglement properties. This behavior may be enhanced in systems that have flat energy bands, such as stacked two-dimensional (2D) materials, for they exaggerate the role of interactions over kinetic energy. To that end, much attention has been devoted to the novel superconducting and insulating phases of twisted bilayer graphene [1–3], which forms flat bands at a set of magic twisting angles [4–10]. The resulting lattice has an enlarged unit cell, forming a so-called moiré superlattice pattern [11–13]. Away from magic angles, twisted models exhibit long-range quasiperiodic order, connecting to the physics of quasicrystals [14–19]. This case is, however, unlike in solid-state bilayers, where commensurability via interactions is strongly favoured during fabrication [11,20,21]. Twisted models can also be emulated in quantum simulators, such as photonic materials [22,23], cavity polaritons [24], and ultracold atoms [25–30]. These systems offer high control over interactions and the underlying geometry of potentials. Moreover, they pave the way to a new class of models, namely, twisted bosonic matter, which has, so far, been little studied compared to fermionic counterparts. Ultracold bosons in simple periodic potentials have been extensively investigated and used to demonstrate Mott-insulator (MI) to superfluid (SF) phase transitions [31,32]. If disorder is present, the Bose glass (BG), a special kind of compressible insulator, can also appear [33–36], and has been observed in both disordered [37–43] and quasiperiodic models [37,44–52]. In recent years, these procedures have also been extended to twisted optical lattices [53–57]. Here, the twist angle can be freely tuned between commensurate and incommensurate values. So far, the role of incommensuration has been discussed in connection with ergodicity breaking in single-particle dynamics [58] and SF-MI transitions in one-dimensional interacting Bose gases [59].

For this Letter, we study the exotic phase diagrams of strongly correlated ultracold bosons within a twisted optical lattice, for both commensurate and incommensurate angles. Using a combination of quantum Monte Carlo (QMC) and exact diagonalization, we show that, in spite of the potentials having a very similar character, both cases behave completely differently. For incommensurate angles, our results confirm the presence of MI, SF, and BG phases, which we find to be closely linked to the localization of single-particle states. For commensurate angles, the BG is replaced by a series of density-waves (DWs), separated by weak SF domains: a thermally unstable SF with low SF fraction at zero temperature. These regions leave behind prominent normal fluid (NF) phases even at low temperature. We show that weak SF phases can, however, be stabilized with the parameters available in current generation experiments.

Model. We consider an interacting, 2D gas of ultracold bosons in an $L \times L$ box, with periodic boundary conditions. The Hamiltonian is

$$\hat{H} = \int d\mathbf{r}\ \hat{\Psi}^\dagger[\hbar^2/2M(-\nabla^2 + \tilde{g}_0\hat{\Psi}^\dagger\hat{\Psi}) + V(\mathbf{r})]\hat{\Psi}, \quad (1)$$

where $\hat{\Psi}$ is the bosonic field operator at point $\mathbf{r} = (x, y)$, M is the atomic mass, $\tilde{g}_0$ is the dimensionless 2D contact interaction strength [60–63], and $V(\mathbf{r})$ is the optical potential. The potential is constructed via two rotated square lattices, with period a,

$$V(\mathbf{r}) = V_1 v(R^-\mathbf{r}) + V_2 v(R^+\mathbf{r}), \quad (2)$$

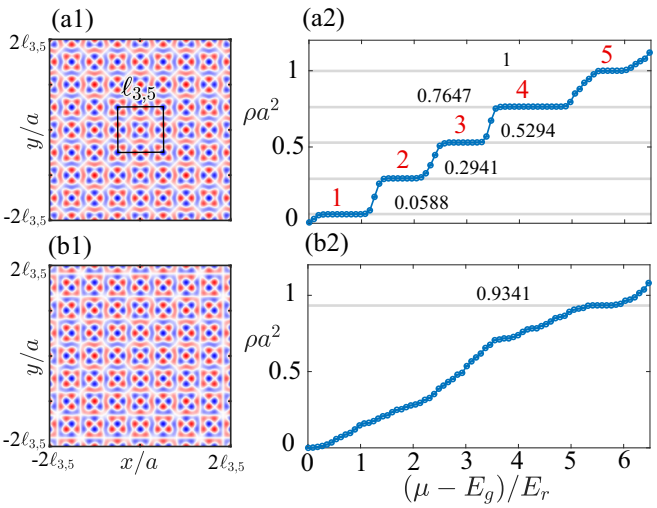

FIG. 1. (a1) Commensurate potential with $\theta_{3,5} \approx 28.07^\circ$ (black square shows the unit cell) and (b1) incommensurate potential with $\theta \approx 27.13^\circ$. (a2), (b2) QMC results for density versus shifted chemical potential at each respective angle for $V = 6E_r$, $\tilde{g}_0 = 4$, $k_B T = 0.04E_r$, and $L = 5\ell_{3,5} \approx 20.62a$. Plateaus in density are marked by grey lines, with $\rho a^2 < 1$ (DW) and $\rho a^2 = 1$ (MI). Red numbers in (a2) denote the index of the plateau p, which has $1 + 4(p-1)$ atoms per unit cell.

where $v(\mathbf{r}) = \cos^2(2\pi x/a) + \cos^2(2\pi y/a)$, $V_{1,2}$ are the potential depths, and $R^{\pm}$ the rotation with angle $\pm\theta/2$. Without loss of generality, we consider cases where $V_1 = V_2 = V$ [64].

All energies will be expressed in terms of the recoil energy $E_r = \pi^2\hbar^2/2Ma^2$. For almost any angle θ, $V(\mathbf{r})$ forms an incommensurate (quasiperiodic) potential. However, for a countable set of commensurate angles $\theta_{m,n}$, it takes the form of a commensurate (periodic) moiré potential. These angles are defined by two coprime integers m and n that sum to an even number [53], with $\theta_{m,n} = \cos^{-1}(\frac{2mn}{m^2+n^2})$, where the length $\ell_{m,n}$ of the square unit cell is given by $\ell_{m,n} = a\sqrt{(m^2+n^2)/2}$. We compare Fig. 1(a1) a commensurate potential for the angle $\theta_{3,5} \approx 28.07^\circ$ with Fig. 1(a2) an incommensurate potential for a small shift in angle to $\theta = 27.13^\circ$. The first is strictly periodic, with period $\ell_{3,5} \simeq 4.12a$, and exhibits an exotic, decorated unit cell. In contrast, the second is not periodic, but shows a very similar potential profile, with hardly visible distortions. These small differences, however, result in markedly distinct quantum phase diagrams.

Many-Body Phases. To calculate the exact phases, we use continuous-space QMC simulations within the grand canonical ensemble (temperature T and chemical potential μ) [65,66]. We compute the average density $\rho = N/L^2$, where N is the total number of particles, the compressibility $\kappa = \partial\rho/\partial\mu$, and the SF fraction $f_s = \Upsilon/\rho$, where Υ is the superfluid stiffness [67]. Note, working in continuous-space allows us to overcome frustration effects of lattice models that would otherwise impede convergence of QMC. Such frustration effects appear due to a mix of positive and negative tunnelings, known in incommensurate potentials [68] and also found here in commensurate cases. We plot the density ρ versus the shifted chemical potential $\mu - E_g$ (E_g is the single-particle ground-state energy) for Fig. 1(a2) commensurate and Fig. 1(b2) incommensurate potentials. We fix $V = 6E_r$, and consider a strongly interacting gas with $\tilde{g}_0 = 4$. Roughly speaking, ultracold atom experiments can reach temperatures of about 10 nK [69–71]. For ^{87}Rb atoms and a typical $a = 350$ nm, it gives $k_B T \approx 0.04E_r$, which we use in the QMC calculations for Fig. 1. Lower ratios of $k_B T/E_r$ may be reached at the same temperature using different atomic species, e.g., ^{40}K, for which $k_B T \approx 0.02E_r$, or ^{7}Li, for which $k_B T \approx 0.0036E_r$.

First, for the commensurate case with $V = 6E_r$ in Fig. 1(a2), five plateaus in density (red numbers) are observed. These correspond to incompressible, insulating phases with $\kappa = 0$, in which we consistently find $f_s = 0$ (not shown). If the dimensionless density ρa^2 is an integer, we have the standard MI phase. Here, we also find noninteger ρa^2 plateaus, indicating a DW phase. This phase is similar in character to those identified in both superlattice [72,73] and quasiperiodic [49,74] tight-binding models. Furthermore, a single DW-like phase was also observed in experiments and mean-field calculations at $\theta_{1,22} \approx 5.21^\circ$ in Ref. [56]. The increments in density are directly related to the geometry of the moiré potential. First, the lowest DW plateau ($p = 1$) fills the lowest potential minima [blue points at the four corners of the unit cell in Fig. 1(a1)], giving one atom per unit cell. The next DW plateau ($p = 2$) fills the second four lowest minima (located near the midpoints of the unit cell edges), giving now $1 + 4 = 5$ atoms per unit cell. This pattern continues for all insulating phases with $\rho a^2 \leqslant 1$. The density for the pth plateau is then $\rho_p = [1 + 4(p-1)]/\ell^2_{m,n}$, corresponding to the black numbers in Figs 1(a2), 1(a3), and the total number of plateaus is $\mathcal{M}_{m,n} = 1 + (\ell^2_{m,n}/a^2 - 1)/4$. For the commensurate potential, we, therefore, have $\ell^2_{3,5} = 17a^2$ and $\mathcal{M}_{3,5} = 5$, consistent with the results of Fig. 1(a2).

Figure 1(b2) shows the counterpart of Fig. 1(a2) for the incommensurate potential. In spite of the strong similarity between the potentials in Figs. 1(a1) and 1(b1), most plateaus are now absent. Comparatively speaking, commensurate angles form a singular, countable set immersed in a continuous range of incommensurate angles, making the appearance of vastly different physical properties for such a small change in θ surprising. To explain this, we note, however, that any incommensurate potential can be approximated by a commensurate one with very large m and n. This implies that $\mathcal{M}_{m,n}$ diverges, so that each plateau becomes vanishingly narrow. The spectral gaps then vanish, and the compressibility is finite. Moreover, the moiré period increases, which weakens phase coherence and induces localization in the incommensurate limit. This forms a BG, with $\kappa > 0$ and $f_s = 0$. Note, a DW with $\rho a^2 \approx 0.93$ survives due to a small single-particle gap in the quasiperiodic potential.

Weak Superfluids. In our calculations, we find $f_s = 0$ for both potentials, consistent with the onset of DW, MI, and BG phases. However, $f_s = 0$ is also found for the commensurate potential in compressible domains, while a SF is to be expected due to the underlying periodicity of the system. The absence of finite f_s may be attributed to the moiré-enhanced lattice period and the finite temperature. In other words, tunneling is vanishingly small, and the system is thus unable to stabilise superfluidity, even against very weak thermal fluctuations.

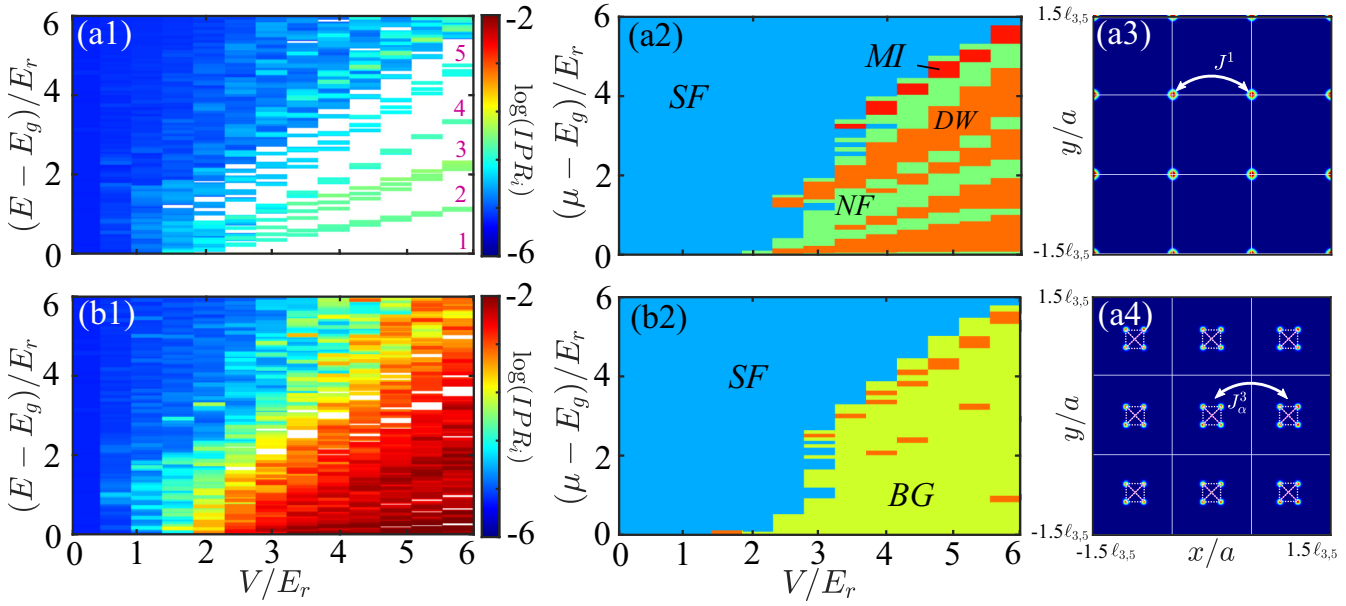

FIG. 2. (a1), (b1) IPR_i of single-particle states for $L = 15\ell_{3,5} \approx 61.85a$, at (a1) commensurate angle with $\theta_{3,5} \approx 28.07^\circ$ and (b1) incommensurate angle with $\theta \approx 27.13^\circ$. (a2), (b2) QMC phase diagrams for the same potentials when $\tilde{g}_0 = 4$, $k_B T = 0.01E_r$, and $L = 5\ell_{3,5} \approx 20.62a$. (a3), (a4) Examples of single-particle states below gap (a3) 1 and (a4) 3 are shown for the commensurate potential, which can be mapped to tight-binding models. J^1 and J^β_α are couplings between states in nearest moiré unit cells (white cells).

To check this, we perform QMC calculations at lower temperature $k_B T = 0.01E_r$, and compare with single-particle properties. Figures 2(a1) and 2(b1) show the single-particle spectra versus energy and potential depth for both commensurate and incommensurate potentials, with $L = 15\ell_{3,5} \approx 61.85a$. The spectra are colored according to the inverse participation ratio $\mathrm{IPR}_i = \int d\mathbf{r}|\psi_i(\mathbf{r})|^4$ of each state i, with blue (red) regions mapping to extended (localized and/or critical) states. Starting with the incommensurate case in Fig. 2(b1), the low-energy states are primarily localized above a critical potential depth (here $V \approx 2.5E_r$), as expected for a quasiperiodic system. The onset of single-particle localization is both qualitatively and quantitatively consistent with the BG phase for the corresponding many-body phase diagram in Fig. 2(b2), while extended states map onto the SF phase. Narrow DW regions, consistent with single-particle gaps, are also visible.

Let us now turn to the commensurate case. The single-particle spectrum in Fig. 2(a1) displays five prominent gaps (labeled 1 to 5), which quantitatively overlap the five insulating plateaus in the many-body phase diagram of Fig. 2(a2) (1 to 4 are DWs, 5 is the MI). This quantitative mapping is to be expected, owing to 2D fermionization of strongly repelling bosons. Here, the single-particle states in different bands occupy separated regions of the plane, so that energy is minimized by filling each with up to one boson, hence mimicking local Pauli exclusion [51,75]. The spatial separation of single-particle states is illustrated in Figs. 2(a3) and 2(a4), which show the density distribution of eigenstates in the first and third band, respectively. In the first band, the density is concentrated at the nodes of the white, moiré unit cells, while in the third band, it is concentrated around four points near the center of each unit cell. Similar separation occurs with the other bands.

Due to periodicity and Bloch's theorem, all states are extended, with the underlying density profiles in Figs. 2(a3) and 2(a4) implying that different bands with index β correspond to different tight-binding geometries [76], see also [77]. For band $\beta = 1$, the picture is straightforward since there is one site per unit cell, see Fig. 2(a3). This yields a standard square lattice with period $\ell_{3,5}$, which has a dispersion relation of

$$\varepsilon(\mathbf{k}) = \epsilon^1 - 2\left[J^1_x \cos(k_x \ell_{3,5}) + J^1_y \cos(k_y \ell_{3,5})\right], \qquad (3)$$

where $J^1_x = J^1_y = J^1$ owing to four-fold rotation symmetry. Here J^1 is the tunneling rate, ϵ^1 is the on-site energy, and $\mathbf{k} = (k_x, k_y)$ spans the first Brillouin zone $[-\pi/\ell_{3,5} \cdots + \pi/\ell_{3,5}]$. For $V \gtrsim 3E_r$, we find that the tight-binding prediction of Eq. (3) is in excellent agreement with the continuous space band structure.

For the other bands, we have a different scenario in which each moiré cell contains four sites, see, for instance, Fig. 2(a4) corresponding to band 3. Intracell couplings dominate over intercell couplings, so that each band splits into four subbands α ($= a, b, c$, and d) with width much smaller than the total band width. The subbands a and d are well separated in energy, and can thus described by a standard tight-binding model, yielding dispersion relations similar to Eq. (3) with $J^\beta_{a,d;x} = J^\beta_{a,d;y} = J^\beta_{a,d}$. In contrast, the subbands b and c are quasidegenerate and the four-fold rotation symmetry is broken due to intercell coupling, i.e. $J^\beta_{b,c;x} \neq J^\beta_{b,c;y}$ [78].

By fitting these dispersion relations to the continuous space band structure, we can then extract all relevant tunneling energies. For $V = 6E_r$, we find that the largest tunneling in each band, $J^\beta_{\max} = \max_\alpha(|J^\beta_\alpha|)$ ranges from $J^1_{\max} \sim 10^{-11}E_r$ to $J^5_{\max} \sim 10^{-3}E_r$ [76].

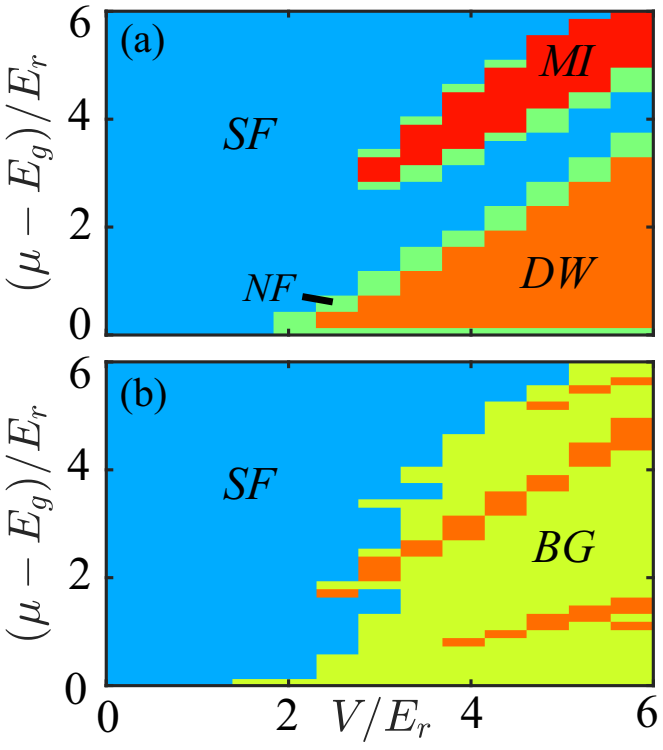

FIG. 3. QMC phase diagrams with $\tilde{g}_0 = 4$, $k_B T = 0.01E_r$, and $L = 10\ell_{3,1} \approx 22.36a$, for the (a) commensurate angle $\theta_{3,1} \approx 36.87^\circ$ and (b) incommensurate angle $\theta \approx 37.82^\circ$.

To observe a distinct SF phase within band β, we typically require that $k_B T \lesssim J^\beta_{\max}$ [79]. For $V = 6E_r$, it means $k_B T \lesssim 0.001E_r$, i.e., for ^{87}Rb atoms $T \lesssim 0.25$ nK, quite unrealistic for present-day experiments. For QMC simulations and typical experiments with $k_B T \approx 0.04E_r$, thermal broadening strongly depletes the SF domains, leaving behind a thermal NF phase, which explains the absence of observable superfluidity in the calculations of Fig. 1. This effect can, however, be somewhat mitigated by considering smaller potential depths, in which the effective couplings J^β_α then become larger. For instance, when $V = 3E_r$, the largest tunnellings culminate to $J^2_{\max} \approx 0.0134E_r$, within band 2. QMC calculations for varying temperatures confirm that a sizable SF fraction appears roughly for $k_B T \sim J^2_{\max}$ [76]. The phase diagrams in Fig. 2 are plotted for $k_B T = 0.01E_r$, slightly below $J^2_{\max}$ and, consistently, a small SF domain appears for $V = 3E_r$ and $(\mu - E_g) \sim 1.5E_r$ in Fig. 2(a2). Due to the small values of J^β_α, however, SF domains between insulators are very narrow and only present around $V = 3E_r$, with thermal fluctuations leading to the prevalence of the NF.

To further enhance the superfluidity between the insulating plateaus without further reducing T or V, we may exploit another controllable parameter of ultracold atoms, namely, the twist angle θ. In Fig. 3(a), we plot another phase diagram for the same parameters as in Fig. 2(a2), but with $\theta = \theta_{3,1} \approx 36.87^\circ$. At this commensurate angle, the size of the unit cell is now $\ell_{3,1} \approx 2.24a$, giving $\mathcal{M}_{3,1} = 2$. We consistently find a single DW lobe (with $\rho a^2 = 0.2$) below the MI (with $\rho a^2 = 1$). The smaller unit cell enhances tunneling rates, which now culminate to $J^2_{\max} = 0.042E_r$ for $V = 6E_r$. We then find a prominent SF phase, leaving behind narrow NF domains around the edges of DW and MI lobes. In between these insulators, we find a low SF fraction, which varies from $f_s \approx 0.2$ at $V = 3E_r$ to $f_s \approx 0.1$ at $V = 6E_r$. The SF phase transition is consistent with a Berezinski-Kosterlitz-Thouless (BKT) mechanism, with a critical temperature in the range $T_c \approx 0.025$–$0.03E_r/k_B$. For the temperature $T = 0.01E_r/k_B$ and the size $L \approx 22.36a$ used here, thermal fluctuations and finite-size effects are strongly suppressed [76]. Our results are thus representative of quantum phase diagrams. Note, weak superfluids are reminiscent of the recently observed SF-II in bilayer Bose systems [56].

Consistently with the results above, a drastic change in behavior is observed for a small angular variation to the incommensurate $\theta \approx 37.82^\circ$ in Fig. 3(b). Large DW and MI lobes vanish, as well as the intermediate SF, leaving behind a BG that is qualitatively similar to that observed for $\theta \approx 27.13^\circ$ in Fig. 2(b2).

Conclusion. We showed that bosonic matter in twisted potentials with controlled twist angle can undergo a variety of exotic phase transitions. Incommensurate angles induce quasiperiodic potentials, which support BG phases over large ranges of potential depths and chemical potentials. In contrast, commensurate angles create moiré potentials, which generates a family of DW lobes. Such insulating domains map onto single-particle gaps, which separate bands and narrow subbands. The narrow subbands support weak superfluids, characterized by low SF fraction at zero temperature and high sensitivity to thermal fluctuations. Sizeable SF domains can, however, be stabilized by controlling the potential depth and, more importantly, the twist angle. Our results are directly applicable to current generation ultracold atom experiments, by using configurations similar to Refs. [45,46,52], where phases can be identified using standard matter-wave interferometry and transport measurements. They may also impact our understanding of fermionic systems in strong-pairing regimes. Finally, our work may be extended to other bosonic quantum simulation platforms using photonic materials or cavity polaritons, where drive-dissipation processes may induce novel effects.

Acknowledgments. We thank Jing Zhang and Shengjie Yu for fruitful discussions. We acknowledge the CPHT computer team for valuable support. This research was supported by the Agence Nationale de la Recherche (ANR, project ANR-CMAQ-002 France 2030), the program "Investissements d'Avenir," the LabEx PALM (Project No. ANR-10-LABX-0039-PALM), the IPParis Doctoral School, the Swiss National Science Foundation (Grants No. 200020-188687 and No. 200020-219400), and HPC/AI resources from GENCI-TGCC (Grant No. 2023-A0110510300) using the ALPS scheduler library and statistical analysis tools [80,81].

[1] Y. Cao, V. Fatemi, S. Fang, K. Watanabe, T. Taniguchi, E. Kaxiras, and P. Jarillo-Herrero, Unconventional superconductivity in magic-angle graphene superlattices, Nature (London) **556**, 43 (2018).

[2] Y. Cao, V. Fatemi, A. Demir, S. Fang, S. L. Tomarken, J. Y. Luo, J. D. Sanchez-Yamagishi, K. Watanabe, T. Taniguchi, E. Kaxiras *et al.*, Correlated insulator behaviour at half-filling in magic-angle graphene superlattices, Nature (London) **556**, 80 (2018).

[3] M. Yankowitz, S. Chen, H. Polshyn, Y. Zhang, K. Watanabe, T. Taniguchi, D. Graf, A. F. Young, and C. R. Dean, Tuning superconductivity in twisted bilayer graphene, Science **363**, 1059 (2019).

[4] E. Suárez Morell, J. D. Correa, P. Vargas, M. Pacheco, and Z. Barticevic, Flat bands in slightly twisted bilayer graphene: Tight-binding calculations, Phys. Rev. B **82**, 121407(R) (2010).

[5] R. Bistritzer and A. H. MacDonald, Moiré bands in twisted double-layer graphene, Proc. Natl. Acad. Sci. **108**, 12233 (2011).

[6] G. Tarnopolsky, A. J. Kruchkov, and A. Vishwanath, Origin of magic angles in twisted bilayer graphene, Phys. Rev. Lett. **122**, 106405 (2019).

[7] H. C. Po, L. Zou, A. Vishwanath, and T. Senthil, Origin of Mott insulating behavior and superconductivity in twisted bilayer graphene, Phys. Rev. X **8**, 031089 (2018).

[8] J. González and T. Stauber, Kohn-luttinger superconductivity in twisted bilayer graphene, Phys. Rev. Lett. **122**, 026801 (2019).

[9] M. Xie and A. H. MacDonald, Nature of the correlated insulator states in twisted bilayer graphene, Phys. Rev. Lett. **124**, 097601 (2020).

[10] Y. Choi, J. Kemmer, Y. Peng, A. Thomson, H. Arora, R. Polski, Y. Zhang, H. Ren, J. Alicea, G. Refael *et al.*, Electronic correlations in twisted bilayer graphene near the magic angle, Nat. Phys. **15**, 1174 (2019).

[11] J. M. B. Lopes dos Santos, N. M. R. Peres, and A. H. Castro Neto, Graphene bilayer with a twist: Electronic structure, Phys. Rev. Lett. **99**, 256802 (2007).

[12] J. M. B. Lopes dos Santos, N. M. R. Peres, and A. H. Castro Neto, Continuum model of the twisted graphene bilayer, Phys. Rev. B **86**, 155449 (2012).

[13] L. Zou, H. C. Po, A. Vishwanath, and T. Senthil, Band structure of twisted bilayer graphene: Emergent symmetries, commensurate approximants, and Wannier obstructions, Phys. Rev. B **98**, 085435 (2018).

[14] D. Shechtman, I. Blech, D. Gratias, and J. W. Cahn, Metallic phase with long-range orientational order and no translational symmetry, Phys. Rev. Lett. **53**, 1951 (1984).

[15] W. Steurer, Twenty years of structure research on quasicrystals. Part I. Pentagonal, octagonal, decagonal and dodecagonal quasicrystals, Z. Kristallogr. Cryst. Mater. **219**, 391 (2004).

[16] W. Steurer, Quasicrystals: what do we know? what do we want to know? what can we know?, Acta Cryst. A **74**, 1 (2018).

[17] K. Kamiya, T. Takeuchi, N. Kabeya, N. Wada, T. Ishimasa, A. Ochiai, K. Deguchi, K. Imura, and N. Sato, Discovery of superconductivity in quasicrystal, Nat. Commun. **9**, 1 (2018).

[18] S. J. Ahn, P. Moon, T.-H. Kim, H.-W. Kim, H.-C. Shin, E. H. Kim, H. W. Cha, S.-J. Kahng, P. Kim, M. Koshino, Y.-W. Son, C.-W. Yang, and J. R. Ahn, Dirac electrons in a dodecagonal graphene quasicrystal, Science **361**, 782 (2018).

[19] W. Yao, E. Wang, C. Bao, Y. Zhang, K. Zhang, K. Bao, C. K. Chan, C. Chen, J. Avila, M. C. Asensio, J. Zhu, and S. Zhou, Quasicrystalline 30° twisted bilayer graphene as an incommensurate superlattice with strong interlayer coupling, Proc. Natl. Acad. Sci. USA **115**, 6928 (2018).

[20] J. Hass, F. Varchon, J. E. Millán-Otoya, M. Sprinkle, N. Sharma, W. A. de Heer, C. Berger, P. N. First, L. Magaud, and E. H. Conrad, Why multilayer graphene on $4h-\mathrm{SiC}(000\bar{1})$ behaves like a single sheet of graphene, Phys. Rev. Lett. **100**, 125504 (2008).

[21] Y. Kim, H. Yun, S.-G. Nam, M. Son, D. S. Lee, D. C. Kim, S. Seo, H. C. Choi, H.-J. Lee, S. W. Lee, and J. S. Kim, Breakdown of the interlayer coherence in twisted bilayer graphene, Phys. Rev. Lett. **110**, 096602 (2013).

[22] A. Majumdar, A. Rundquist, M. Bajcsy, V. D. Daisika, S. R. Bank, and J. Vuckovic, Design and analysis of photonic crystal coupled cavity arrays for quantum simulation, Phys. Rev. B **86**, 195312 (2012).

[23] N. C. Harris, M. Prabhu, G. R. Steinbrecher, Y. Lahini, J. Mower, D. Bunandar, C. Chen, F. N. C. Wong, T. Baehr-Jones, M. Hochberg, S. Lloyd, and D. Englund, Quantum transport simulations in a programmable nanophotonic processor, Nat. Photonics **11**, 447 (2017).

[24] I. Carusotto and C. Ciuti, Quantum fluids of light, Rev. Mod. Phys. **85**, 299 (2013).

[25] M. Lewenstein, A. Sanpera, V. Ahufinger, B. Damski, A. Sen(De), and U. Sen, Ultracold atomic gases in optical lattices: mimicking condensed matter physics and beyond, Adv. Phys. **56**, 243 (2007).

[26] I. Bloch, J. Dalibard, and W. Zwerger, Many-body physics with ultracold gases, Rev. Mod. Phys. **80**, 885 (2008).

[27] C. Gross and I. Bloch, Quantum simulations with ultracold atoms in optical lattices, Science **357**, 995 (2017).

[28] O. Dutta, M. Gajda, P. Hauke, M. Lewenstein, D.-S. Lühmann, B. A. Malomed, T. Sowiński, and J. Zakrzewski, Non-standard Hubbard models in optical lattices: A review, Rep. Prog. Phys. **78**, 066001 (2015).

[29] T. Esslinger, Fermi-Hubbard physics with atoms in an optical lattice, Annu. Rev. Condens. Matter Phys. **1**, 129 (2010).

[30] L. Tarruell and L. Sanchez-Palencia, Quantum simulation of the Hubbard model with ultracold fermions in optical lattices, C. R. Phys. **19**, 365 (2018).

[31] D. Jaksch, C. Bruder, J. I. Cirac, C. W. Gardiner, and P. Zoller, Cold bosonic atoms in optical lattices, Phys. Rev. Lett. **81**, 3108 (1998).

[32] M. Greiner, O. Mandel, T. Esslinger, T. W. Hänsch, and I. Bloch, Quantum phase transition from a superfluid to a Mott insulator in a gas of ultracold atoms, Nature (London) **415**, 39 (2002).

[33] T. Giamarchi and H. J. Schulz, Localization and interactions in one-dimensional quantum fluids, Europhys. Lett. **3**, 1287 (1987).

[34] T. Giamarchi and H. J. Schulz, Anderson localization and interactions in one-dimensional metals, Phys. Rev. B **37**, 325 (1988).

[35] M. P. A. Fisher, P. B. Weichman, G. Grinstein, and D. S. Fisher, Boson localization and the superfluid-insulator transition, Phys. Rev. B **40**, 546 (1989).

[36] J. Kisker and H. Rieger, Bose-glass and Mott-insulator phase in the disordered boson Hubbard model, Phys. Rev. B **55**, R11981(R) (1997).

[37] B. Damski, J. Zakrzewski, L. Santos, P. Zoller, and M. Lewenstein, Atomic Bose and Anderson glasses in optical lattices, Phys. Rev. Lett. **91**, 080403 (2003).

[38] P. Lugan, D. Clément, P. Bouyer, A. Aspect, M. Lewenstein, and L. Sanchez-Palencia, Ultracold Bose gases in 1D disorder: From Lifshits glass to Bose-Einstein condensate, Phys. Rev. Lett. **98**, 170403 (2007).

[39] P. Lugan, D. Clément, P. Bouyer, A. Aspect, and L. Sanchez-Palencia, Anderson localization of Bogolyubov quasiparticles in interacting Bose-Einstein condensates, Phys. Rev. Lett. **99**, 180402 (2007).

[40] V. Gurarie, L. Pollet, N. V. Prokof'ev, B. V. Svistunov, and M. Troyer, Phase diagram of the disordered Bose-Hubbard model, Phys. Rev. B **80**, 214519 (2009).

[41] S. G. Söyler, M. Kiselev, N. V. Prokof'ev, and B. V. Svistunov, Phase diagram of the commensurate two-dimensional disordered Bose-Hubbard model, Phys. Rev. Lett. **107**, 185301 (2011).

[42] G. Carleo, G. Boéris, M. Holzmann, and L. Sanchez-Palencia, Universal superfluid transition and transport properties of two-dimensional dirty bosons, Phys. Rev. Lett. **111**, 050406 (2013).

[43] L. Sanchez-Palencia and M. Lewenstein, Disordered quantum gases under control, Nat. Phys. **6**, 87 (2010).

[44] L. Fallani, J. E. Lye, V. Guarrera, C. Fort, and M. Inguscio, Ultracold atoms in a disordered crystal of light: Towards a Bose glass, Phys. Rev. Lett. **98**, 130404 (2007).

[45] K. Viebahn, M. Sbroscia, E. Carter, J.-C. Yu, and U. Schneider, Matter-wave diffraction from a quasicrystalline optical lattice, Phys. Rev. Lett. **122**, 110404 (2019).

[46] M. Sbroscia, K. Viebahn, E. Carter, J.-C. Yu, A. Gaunt, and U. Schneider, Observing localization in a 2D quasicrystalline optical lattice, Phys. Rev. Lett. **125**, 200604 (2020).

[47] H. Yao, T. Giamarchi, and L. Sanchez-Palencia, Lieb-Liniger bosons in a shallow quasiperiodic potential: Bose glass phase and fractal Mott lobes, Phys. Rev. Lett. **125**, 060401 (2020).

[48] R. Gautier, H. Yao, and L. Sanchez-Palencia, Strongly interacting bosons in a two-dimensional quasicrystal lattice, Phys. Rev. Lett. **126**, 110401 (2021).

[49] D. Johnstone, P. Öhberg, and C. W. Duncan, Barriers to macroscopic superfluidity and insulation in a 2D Aubry–André model, J. Phys. B: At. Mol. Opt. Phys. **55**, 125302 (2022).

[50] D. Johnstone, P. Öhberg, and C. W. Duncan, The mean-field Bose glass in quasicrystalline systems, J. Phys. A: Math. Theor. **54**, 395001 (2021).

[51] Z. Zhu, H. Yao, and L. Sanchez-Palencia, Thermodynamic phase diagram of two-dimensional bosons in a quasicrystal potential, Phys. Rev. Lett. **130**, 220402 (2023).

[52] J.-C. Yu, S. Bhave, L. Reeve, B. Song, and U. Schneider, Observing the two-dimensional Bose glass in an optical quasicrystal, Nature **633**, 338 (2024).

[53] A. González-Tudela and J. I. Cirac, Cold atoms in twisted-bilayer optical potentials, Phys. Rev. A **100**, 053604 (2019).

[54] T. Salamon, A. Celi, R. W. Chhajlany, I. Frérot, M. Lewenstein, L. Tarruell, and D. Rakshit, Simulating twistronics without a twist, Phys. Rev. Lett. **125**, 030504 (2020).

[55] X.-W. Luo and C. Zhang, Spin-twisted optical lattices: Tunable flat bands and Larkin-Ovchinnikov superfluids, Phys. Rev. Lett. **126**, 103201 (2021).

[56] Z. Meng, L. Wang, W. Han, F. Liu, K. Wen, C. Gao, P. Wang, C. Chin, and J. Zhang, Atomic Bose–Einstein condensate in twisted-bilayer optical lattices, Nature (London) **615**, 231 (2023).

[57] J. Lee and J. H. Pixley, Emulating twisted double bilayer graphene with a multiorbital optical lattice, SciPost Phys. **13**, 033 (2022).

[58] G. C. Paul, P. Recher, and L. Santos, Particle dynamics and ergodicity-breaking in twisted-bilayer optical lattices, Phys. Rev. A **108**, 053305 (2023).

[59] H. Yao, L. Tanzi, L. Sanchez-Palencia, T. Giamarchi, G. Modugno, and C. D'Errico, Mott transition for a Lieb-Liniger gas in a shallow quasiperiodic potential: Delocalization induced by disorder, Phys. Rev. Lett. **133**, 123401 (2024).

[60] D. S. Petrov, M. Holzmann, and G. V. Shlyapnikov, Bose-einstein condensation in quasi-2d trapped gases, Phys. Rev. Lett. **84**, 2551 (2000).

[61] D. S. Petrov and G. V. Shlyapnikov, Interatomic collisions in a tightly confined Bose gas, Phys. Rev. A **64**, 012706 (2001).

[62] L. Pricoupenko and M. Olshanii, Stability of two-dimensional Bose gases in the resonant regime, J. Phys. B: At. Mol. Opt. Phys. **40**, 2065 (2007).

[63] L.-C. Ha, C.-L. Hung, X. Zhang, U. Eismann, S.-K. Tung, and C. Chin, Strongly interacting two-dimensional Bose gases, Phys. Rev. Lett. **110**, 145302 (2013).

[64] Further calculations for the unbalanced case, $V_1 \neq V_2$, not shown in this work, yield the same phases as discussed here and qualitatively similar phase diagrams.

[65] M. Boninsegni, N. Prokof'ev, and B. Svistunov, Worm algorithm for continuous-space path integral Monte Carlo simulations, Phys. Rev. Lett. **96**, 070601 (2006).

[66] M. Boninsegni, N. V. Prokof'ev, and B. V. Svistunov, Worm algorithm and diagrammatic Monte Carlo: A new approach to continuous-space path integral Monte Carlo simulations, Phys. Rev. E **74**, 036701 (2006).

[67] D. M. Ceperley, Path integrals in the theory of condensed helium, Rev. Mod. Phys. **67**, 279 (1995).

[68] E. Gottlob and U. Schneider, Hubbard models for quasicrystalline potentials, Phys. Rev. B **107**, 144202 (2023).

[69] C. Li, T. Zhou, I. Mazets, H.-P. Stimming, F. S. Møller, Z. Zhu, Y. Zhai, W. Xiong, X. Zhou, X. Chen, and J. Schmiedmayer, Relaxation of bosons in one dimension and the onset of dimensional crossover, SciPost Phys. **9**, 058 (2020).

[70] N. Fabbri, D. Clément, L. Fallani, C. Fort, and M. Inguscio, Momentum-resolved study of an array of one-dimensional strongly phase-fluctuating Bose gases, Phys. Rev. A **83**, 031604(R) (2011).

[71] N. Fabbri, M. Panfil, D. Clément, L. Fallani, M. Inguscio, C. Fort, and J.-S. Caux, Dynamical structure factor of one-dimensional Bose gases: Experimental signatures of beyond-luttinger-liquid physics, Phys. Rev. A **91**, 043617 (2015).

[72] V. G. Rousseau, D. P. Arovas, M. Rigol, F. Hébert, G. G. Batrouni, and R. T. Scalettar, Exact study of the one-dimensional boson Hubbard model with a superlattice potential, Phys. Rev. B **73**, 174516 (2006).

[73] B.-L. Chen, S.-P. Kou, Y. Zhang, and S. Chen, Quantum phases of the Bose-Hubbard model in optical superlattices, Phys. Rev. A **81**, 053608 (2010).

[74] G. Roux, T. Barthel, I. P. McCulloch, C. Kollath, U. Schollwöck, and T. Giamarchi, Quasiperiodic Bose-Hubbard model and localization in one-dimensional cold atomic gases, Phys. Rev. A **78**, 023628 (2008).

[75] Z. Zhu, S. Yu, D. Johnstone, and L. Sanchez-Palencia, Localization and spectral structure in two-dimensional quasicrystal potentials, Phys. Rev. A **109**, 013314 (2024).

[76] See Supplemental Material at http://link.aps.org/supplemental/10.1103/PhysRevResearch.6.L042066 for a discussion on the extraction of tunnelling rates from effective tight-binding models, the finite-temperature, and finite-size behavior or convergence of the SF domains.

[77] D. Johnstone, S. Mishra, Z. Zhu, and L. Sanchez-Palencia, Effective tight-binding models in optical moiré potentials, arXiv:2410.21371.

[78] Note that the global four-fold rotation symmetry is, however, preserved since $J^{\beta}_{b;x} = J^{\beta}_{c;y}$ and $J^{\beta}_{b;y} = J^{\beta}_{c;x}$.

[79] F. Gerbier, Boson Mott insulators at finite temperatures, Phys. Rev. Lett. **99**, 120405 (2007).

[80] M. Troyer, B. Ammon, and E. Heeb, Parallel object oriented Monte Carlo simulations, Lect. Notes Comput. Sci. **1505**, 191 (1998).

[81] B. Bauer, L. D. Carr, H. Evertz, A. Feiguin, J. Freire, S. Fuchs, L. Gamper, J. Gukelberger, E. Gull, S. Guertler, A. Hehn, R. Igarashi, S. Isakov, D. Koop, P. Ma, P. Mates, H. Matsuo, O. Parcollet, G. Pawlowski, J. Picon, L. Pollet, E. Santos, V. Scarola, U. Schollwöck, C. Silva, B. Surer, S. Todo, S. Trebst, M. Troyer, M. Wall, P. Werner, and S. Wessel, The ALPS project release 2.0: Open source software for strongly correlated systems, J. Stat. Mech.: Th. Exp. (2011) P05001.

Supplemental Material for Weak Superfluidity in Twisted Optical Potentials

Dean Johnstone,[1] Shanya Mishra,[1] Zhaoxuan Zhu,[1] Hepeng Yao,[2] and Laurent Sanchez-Palencia[1]

[1] *CPHT, CNRS, Ecole Polytechnique, IP Paris, F-91128 Palaiseau, France*

[2] *DQMP, University of Geneva, 24 Quai Ernest-Ansermet, CH-1211 Geneva, Switzerland*

(Dated: November 22, 2024)

This supplemental material gives details about the construction of band-dependent tight-binding models and the extraction of effective tunnelling energies (Sec. I), the finite temperature behaviour of the SF domains (Sec. II) and the finite-size scaling of weak superfluid domains (Sec. III).

I. Band-dependent effective tight-binding models

To determine the tunnelling energies in periodic moiré potentials, we compare the energy spectra as found using continuous-space exact diagonalization of the single-particle Hamiltonian and the prediction of effective tight-binding models. On the one hand, we calculate the exact dispersion relations $\varepsilon(\mathbf{k})$, with $\mathbf{k}$ the quasi-momentum, by applying the Bloch transform $\psi(\mathbf{r}) = e^{i\mathbf{k}\cdot\mathbf{r}}u(\mathbf{r})$ and solving the Schrödinger-like equation for $u(\mathbf{r})$ within a single unit cell, with length $L = \ell_{3,5}$. Figure S1(a1) shows the single-particle spectrum $\varepsilon(\mathbf{k})$ hence obtained for the commensurate potential with $V = 6E_\mathrm{r}$, across the high symmetry points of the first Brillouin zone, i.e. $\Gamma \to \mathbf{k} = (-\pi/\ell_{3,5}, -\pi/\ell_{3,5})$, $X \to \mathbf{k} = (+\pi/\ell_{3,5}, -\pi/\ell_{3,5})$ and $M \to \mathbf{k} = (+\pi/\ell_{3,5}, +\pi/\ell_{3,5})$. For sufficiently large potential depths V, the single-particle spectrum splits into distinct energy bands, where eigenstates fill degenerate local minima of the potential consecutively, see for instance Figs. 2(a3) and (a4) of the main paper. The ground-state band corresponds to the filling of the degenerate global minima arranged in a simple square lattice and displays the standard cosine-like dispersion of Eq. (6) in the main paper, the width of which yields the tunnelling energy, as discussed in the main paper.

The other bands split into distinct subbands. Each one displays a cosine-like dispersion relation, although some of them are distorted, see zooms given for band 3 in Figs. S1(a2)-(a4). To understand this, we note that the eigenstates now correspond to the filling of 4 local minima within each unit cell. To model this structure in band β, we first separate tunnelling energies between sites/spots into two distinct energy scales: tunnellings within a unit cell, noted with an I, and tunnellings between adjacent unit cells, noted as J_α, where α labels the subband index (the band index β is omitted to simplify notations). In general, intra-cell couplings are much larger than inter-cell couplings, which allows us to treat the latter in perturbation of the former. Within a unique cell, we simply have a 4 sites, with an example in Fig. 2(a4) of the main paper for band 3. Taking I as the nearest-neighbour tunnelling and I' as the next-nearest-neighbour tunnelling, the Hamiltonian can be written as

$$\hat{H} = \begin{pmatrix} \epsilon & -I & -I' & -I \\ -I & \epsilon & -I & -I' \\ -I' & -I & \epsilon & -I \\ -I & -I' & -I & \epsilon \end{pmatrix}, \tag{S1}$$

with ϵ the on-site energy. This matrix has eigenvalues

$$\begin{aligned} E_a &= \epsilon + 2I - I', \\ E_{B,C} &= \epsilon + I', \\ E_d &= \epsilon - 2I - I', \end{aligned} \tag{S2}$$

with degeneracy $E_B = E_C$. To capture tunnelling between sites in different unit cells, we then treat the problem as a lattice of coupled 4-level systems, arranged as a square lattice with period $\ell_{3,5}$. The 4-level system corresponds to the 4 eigenstates of the matrix in Eq. (S1) and the inter-cell couplings are level-dependent. Energy-separation between the subbands allows us to restrict to couplings between equal energy eigenstates. It allows us to write an effective Hamiltonian of the form of

$$\begin{aligned} \hat{H} = {} & E_a \sum_i \hat{a}_i^\dagger \hat{a}_i - J_a \sum_{\langle i,j \rangle} \hat{a}_i^\dagger \hat{a}_j + E_d \sum_i \hat{d}_i^\dagger \hat{d}_i - J_d \sum_{\langle i,j \rangle} \hat{d}_i^\dagger \hat{d}_j \\ & + E_B \sum_i (\hat{B}_i^\dagger \hat{B}_i + \hat{C}_i^\dagger \hat{C}_i) - J_B \sum_{\langle i,j \rangle} (\hat{B}_i^\dagger \hat{B}_j + \hat{C}_i^\dagger \hat{C}_j) - \sum_{\langle i,j \rangle} J'_{B;i,j} (\hat{B}_i^\dagger \hat{C}_j + \hat{C}_i^\dagger \hat{B}_j), \end{aligned} \tag{S3}$$

where i and j span the lattice sites, $\langle i,j\rangle$ denotes nearest-neighbour summations, and the operators $\hat{a}_i$, $\hat{B}_i$, $\hat{C}_i$, and $\hat{d}_i$ annihilate a particle in the corresponding eigenstate of Eq. (S1). Note that the coupling $J'_{B;i,j}$ between the two distinct states $|B\rangle$ and $|C\rangle$ depends on the direction, owing to the symmetry breaking induced by the choice of those states but, due to 4-fold rotational symmetry, we necessary have $J'_{B;x} = -J'_{B;y} \equiv J'_B$, with x and y denoting the tunnelling across the x and y axis. By transforming the operators to momentum space, we then have

$$\hat{H} = \sum_{\mathbf{k}} \varepsilon_a(\mathbf{k})\hat{a}^\dagger_{\mathbf{k}}\hat{a}_{\mathbf{k}} + \sum_{\mathbf{k}} \varepsilon_d(\mathbf{k})\hat{d}^\dagger_{\mathbf{k}}\hat{d}_{\mathbf{k}} + \sum_{\mathbf{k}} \varepsilon_B(\mathbf{k})(\hat{B}^\dagger_{\mathbf{k}}\hat{B}_{\mathbf{k}} + \hat{C}^\dagger_{\mathbf{k}}\hat{C}_{\mathbf{k}}) + \sum_{\mathbf{k}} \varepsilon'_B(\mathbf{k})(\hat{C}^\dagger_{\mathbf{k}}\hat{B}_{\mathbf{k}} + \hat{B}^\dagger_{\mathbf{k}}\hat{C}_{\mathbf{k}}), \tag{S4}$$

where

$$\begin{aligned}
\varepsilon_a(\mathbf{k}) &= E_a - 2J_a\left[\cos(k_x\ell_{3,5}) + \cos(k_y\ell_{3,5})\right], \\
\varepsilon_B(\mathbf{k}) &= E_B - 2J_B\left[\cos(k_x\ell_{3,5}) + \cos(k_y\ell_{3,5})\right], \\
\varepsilon'_B(\mathbf{k}) &= -2J'_B\left[\cos(k_x\ell_{3,5}) - \cos(k_y\ell_{3,5})\right], \\
\varepsilon_d(\mathbf{k}) &= E_d - 2J_d\left[\cos(k_x\ell_{3,5}) + \cos(k_y\ell_{3,5})\right].
\end{aligned} \tag{S5}$$

We may then diagonalise the summation involving $\hat{B}_{\mathbf{k}}$ and $\hat{C}_{\mathbf{k}}$ operator introducing the new operators

$$\hat{b}_{\mathbf{k}} = (\hat{B}_{\mathbf{k}} + \hat{C}_{\mathbf{k}})/\sqrt{2} \qquad \text{and} \qquad \hat{c}_{\mathbf{k}} = (\hat{B}_{\mathbf{k}} - \hat{C}_{\mathbf{k}})/\sqrt{2}, \tag{S6}$$

which allows us to rewrite Eq. (S4) as

$$\hat{H} = \sum_{\mathbf{k}} \varepsilon_a(\mathbf{k})\hat{a}^\dagger_{\mathbf{k}}\hat{a}_{\mathbf{k}} + \sum_{\mathbf{k}} \varepsilon_d(\mathbf{k})\hat{d}^\dagger_{\mathbf{k}}\hat{d}_{\mathbf{k}} + \sum_{\mathbf{k}} \varepsilon_b(\mathbf{k})\hat{b}^\dagger_{\mathbf{k}}\hat{b}_{\mathbf{k}} + \sum_{\mathbf{k}} \varepsilon_c(\mathbf{k})\hat{c}^\dagger_{\mathbf{k}}\hat{c}_{\mathbf{k}}, \tag{S7}$$

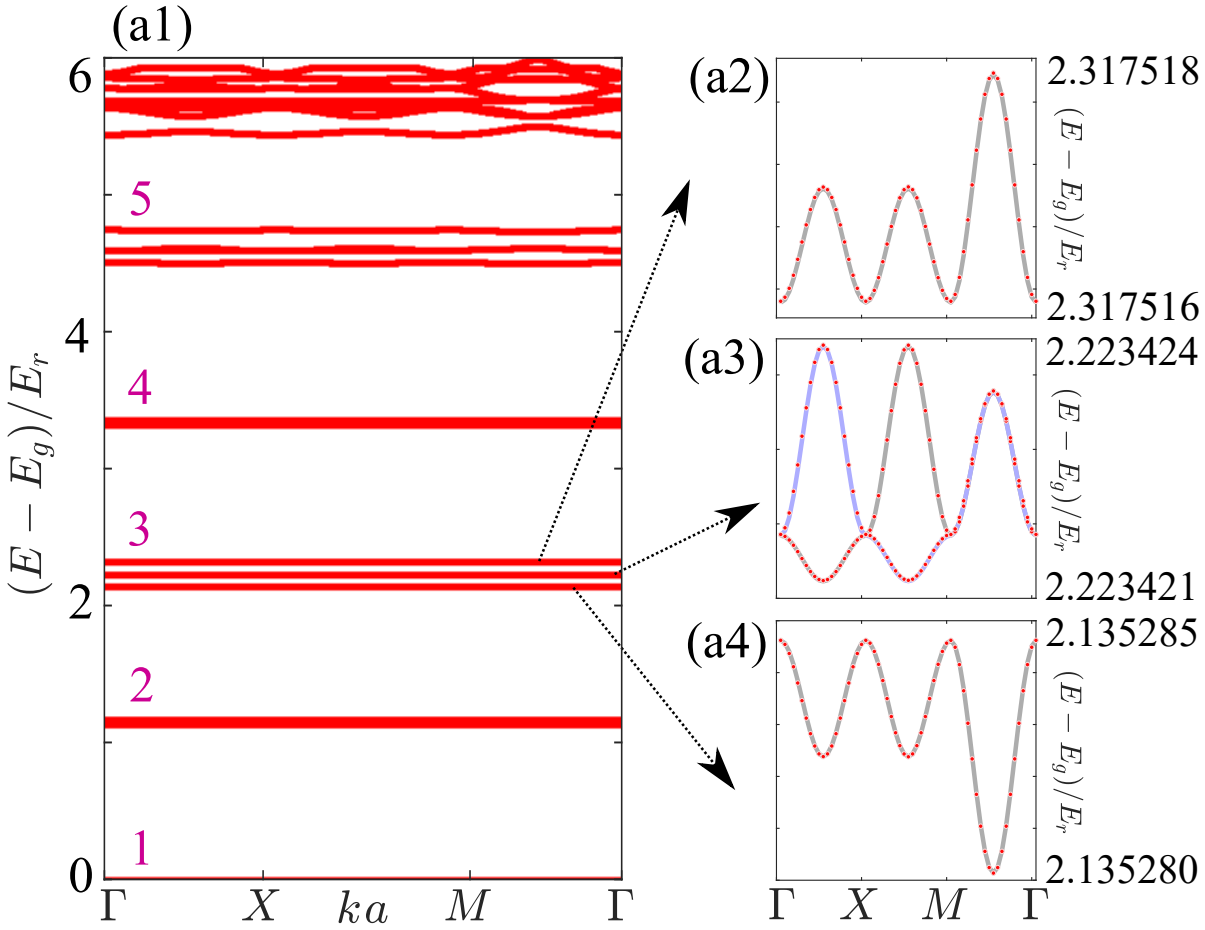

Figure S1. (a1) Low-energy single-particle spectrum for the commensurate potential with $\theta = \theta_{3,5} \approx 28.07°$ and $V = 6E_r$, along high symmetry points of the first Brillouin zone. (a2)-(a4) Zooms in to the subbands of band $\beta = 3$.

where

$$\begin{aligned}\varepsilon_b(\mathbf{k}) &= E_B - 2\big[J_b\cos(k_x\ell_{3,5}) + J_c\cos(k_y\ell_{3,5})\big],\\ \varepsilon_c(\mathbf{k}) &= E_B - 2\big[J_c\cos(k_x\ell_{3,5}) + J_b\cos(k_y\ell_{3,5})\big].\end{aligned} \tag{S8}$$

and

$$J_b = J_B + J'_B \qquad \text{and} \qquad J_c = J_B - J'_B. \tag{S9}$$

Note that, while each band b and c breaks the 4-fold rotation symmetry, the set of both restores it.

Finally, by fitting $\varepsilon_a(\mathbf{k})$, $\varepsilon_b(\mathbf{k})$, $\varepsilon_c(\mathbf{k})$, and $\varepsilon_d(\mathbf{k})$ to the continuous dispersion relations of each subband found from diagonalization of the continuous-space Schrödinger equation, we are then able to determine all of the inter-cell couplings J and J' of the effective lattice model for different bands β. In Table I, we give the largest (J^β_{max}) and smallest (J^β_{min}) inter-cell couplings hence found for each band.

Band	$J^\beta_{\text{min}}/E_\text{r}$	$J^\beta_{\text{max}}/E_\text{r}$
1	4.40×10^{-11}	4.40×10^{-11}
2	8.34×10^{-10}	1.24×10^{-6}
3	7.89×10^{-7}	1.12×10^{-6}
4	2.84×10^{-4}	2.91×10^{-4}
5	2.70×10^{-3}	4.09×10^{-3}

Table I. Tunnelling coefficients of the effective lattice models for the five lowest-energy bands of the commensurate potential with twist angle $\theta_{3,5}$ and amplitude $V = 6E_\text{r}$.

II. Finite-temperature behaviour of weak superfluid domains

Here, we show results for the behaviour of weak SF domains as a function of temperature. In Fig. S2, we plot the (a1) superfluid fraction f_s and (a2) compressibility κ across the phase diagram for the commensurate potential (Fig. 2(a2) from the main paper), for the fixed potential amplitude $V = 3E_\text{r}$. As expected, we find that a sizeable f_s appears roughly when $k_\text{B}T$ is of the order of $J^2_{\text{max}} \approx 0.0134E_\text{r}$ (i.e. $k_\text{B}T/E_\text{r} \approx 0.03 \pm 0.01$). Starting with the larger temperature of $T = 0.04E_\text{r}/k_\text{B}$ (yellow curve) in Figs. S2(a1)-(a2), we find a broad region with $f_\text{s} = 0$ and $\kappa > 0$, clearly indicating the presence of a NF. By decreasing the temperature, we find that a SF domain appears with increasing f_s, slowly growing in width across μ. Furthermore, towards the left and right hand sides of Fig. S2(a2), insulating regions, in which $\kappa = 0$, are also stabilised when the temperature decreases, corresponding to the onset of DW plateaus. The remaining NF domains in which $\kappa > 0$ and $f_\text{s} = 0$ therefore become smaller for decreasing $k_\text{B}T/E_\text{r}$, as expected. Near by $\mu - E_g \approx 1$, we find a peak in compressibility. We expect that it becomes a SF but only at even lower temperatures.

The counterparts for the incommensurate potential (corresponding to Fig. 2(b2) from the main paper) is shown in Figs. S2(b1)-(b2). Here we observe different behaviour: The SF fraction f_s remains vanishingly small, except in a small domain where it is finite for the smaller temperatures $T \leq 0.01E_\text{r}/k_\text{B}$, with values an order of magnitude smaller than that for the commensurate case. The compressibility is non-zero at each point, and the regions with $f_\text{s} = 0$ and $\kappa > 0$ correspond to a BG.

III. Finite-size scaling of weak superfluid domains

To verify that the properties of weak superfluids are well converged in our QMC calculations, we consider both finite-size and finite-temperature effects. In Fig S3, we plot the superfluid fraction f_s (left column) and rescaled superfluid density $n_s\lambda_T^2$ (right column) as a function of temperature for various system lengths and fixed values of the chemical potential. Here $n_s = f_\text{s}\rho$ and $\lambda_T = \sqrt{2\pi\hbar^2/Mk_\text{B}T}$ is the thermal de-Brogile wavelength. We consider the potential amplitude $V = 4E_\text{r}$ for 3 system sizes at 3 chemical potentials between the DW and MI phase from Fig. 3(a) in the main paper, i.e. a weak SF domain. For each case, we observe that f_s converges towards a fixed value $f_\text{s} < 0.2$ as $T \to 0$. In particular, for the results are well converge at the temperature $T = 0.01E_\text{r}/k_\text{B}$ used in the

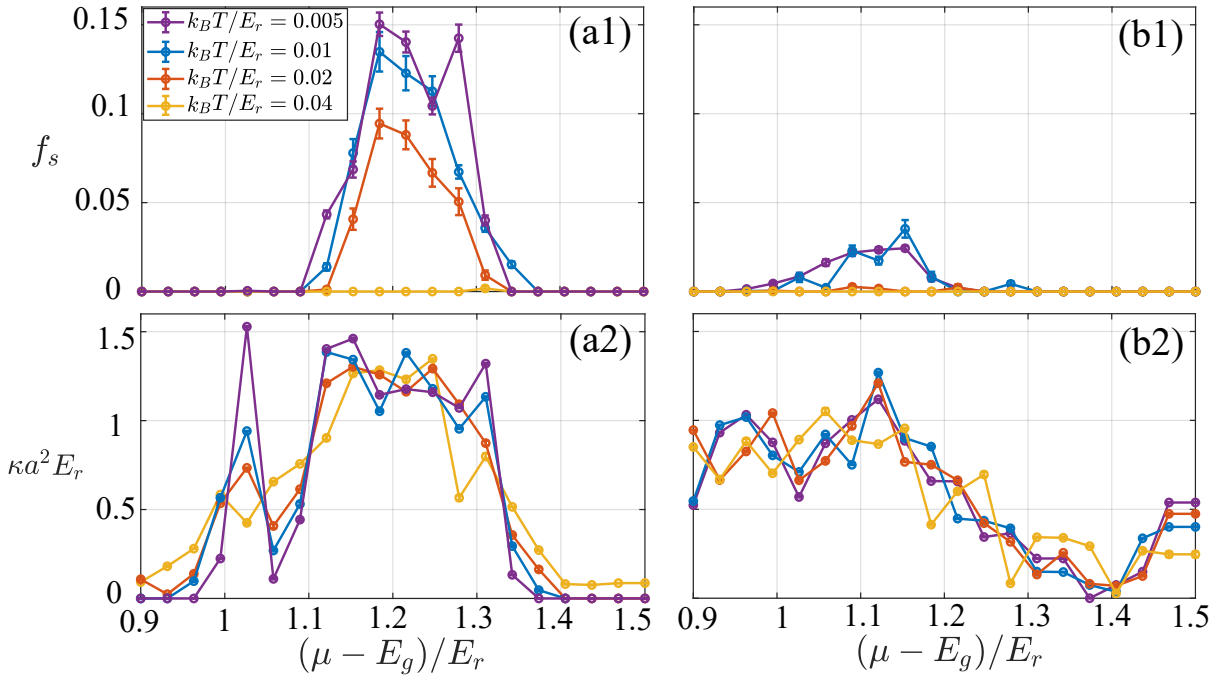

Figure S2. (a1)-(b1) Superfluid fraction f_s and (a2)-(b2) compressibility κ across a small range of μ for the same parameters as Figs. 2(a2) and (b2) of the main paper when $V = 3E_r$, for the commensurate (a1)-(a2) and incommensurate (b1)-(b2) angle respectively.

calculations of the main paper. This shows that weak-superfluidity is retained. It contrasts the usual behaviour that would be expected for a clean (homogeneous) SF phase, in which f_s would converge towards unity as $T \to 0$ [1].

Moreover, we find that below some critical temperatures in the range $T_c \approx 0.02 - 0.03\ E_r/k_B$, the SF fraction at different system sizes generally coincide with another. This shows that finite-size effects are not important in this regime. In some cases, we observe significant fluctuations but they do not alter the phase diagrams of the main paper. In contrast, above the critical temperatures, we find that the curves at different lengths follow a clear trend, with the superfluid fraction decreasing with system size, resulting in a NF. This behaviour is reminiscent of a Berezinski-Kosterlitz-Thouless (BKT) transition, which we verify in Figs. S3(b1)-(b3) by plotting the rescaled superfluid density $n_s\lambda_T^2$ for a slightly smaller range of temperatures. We find a behaviour consistent with a jump close to the the universal jump expected in a clean system, $n_s\lambda_T^2 \approx 4$ [2]. The critical temperatures for the superfluid fraction f_s convergence for each system size in Figs. S3(a1)-(a3) corresponds to $n_s\lambda_T^2 \approx 4$. Similar to before, when we are above T_c, the rescaled superfluid density $n_s\lambda_T^2$ is sensitive to finite-size effects. On the other hand, below T_c, different superfluid density curves will follow similar trends, with no obvious finite-size effects. Our results suggests that the SF transition belongs to the BKT class. A detailed study of the transition is, however, beyond the scope of our work.

In summary, these results show that the phase diagrams presented in our study are representative of the true quantum phase diagrams, with weak SF behaviour persisting in the thermodynamic limit.

[1] N. Prokof'ev and B. Svistunov, Phys. Rev. A **66**, 043608 (2002).
[2] D. R. Nelson and J. M. Kosterlitz, Phys. Rev. Lett. **39**, 1201 (1977).

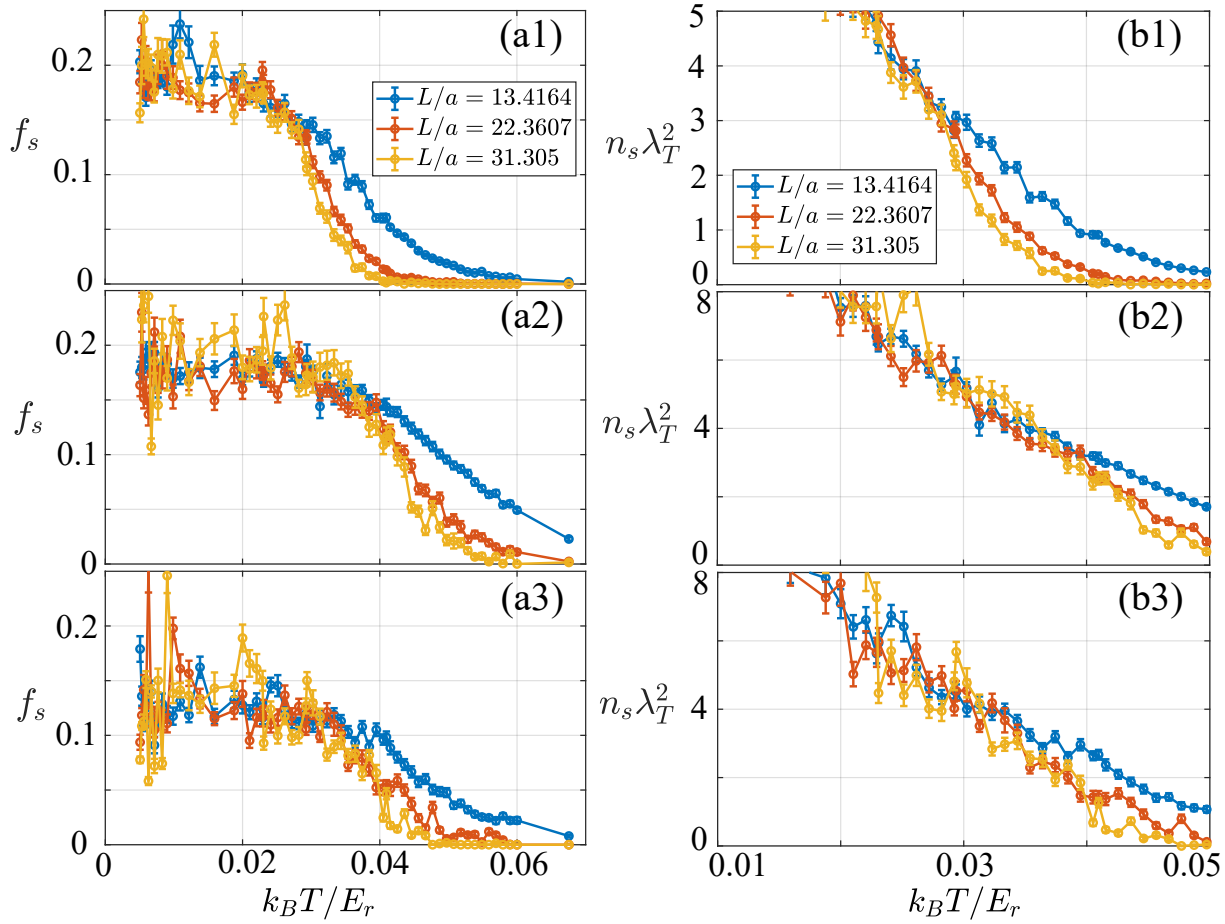

Figure S3. Behaviour of weak superfluids versus temperature and system size. (a1)-(a3) Superfluid fraction f_s and (b1)-(b3) rescaled superfluid density $n_s\lambda_T^2$ for a range of temperatures T and three different system-sizes L, using the same parameters as Fig. 3(a) in the main paper for $V = 4E_r$. We fix (a1),(b1) $(\mu - E_g)/E_r = 1.82$, (a2),(b2) $(\mu - E_g)/E_r = 2.12$ and (a3),(b3) $(\mu - E_g)/E_r = 2.42$.